Published in final edited form as:

Nat Neurosci. 2018 September ; 21(9): 1272–1280. doi:10.1038/s41593-018-0211-4.

In vivo measurement of afferent activity with axon-specific calcium imaging

Gerard Joey Broussard[1], **Yajie Liang**[2], **Marina Fridman**[3], **Elizabeth K. Unger**[1], **Guanghan Meng**[2,4], **Xian Xiao**[1,5], **Na Ji**[2,4], **Leopoldo Petreanu**[3], **Lin Tian**[1]

[1]Department of Biochemistry and Molecular Medicine, University of California Davis, Davis, CA, USA

[2]Janelia Research Campus, Howard Hughes Medical Institute, Ashburn, VA, USA

[3]Champalimaud Center for the Unknown, Lisbon, Portugal

[4]Department of Physics, Department of Molecular & Cellular Biology, University of California Berkeley, Berkeley, CA, USA

[5]Westlake Institute for Advanced Study, Hangzhou, China

Abstract

In vivo calcium imaging from axons provides direct interrogation of afferent neural activity, informing neural representations that a local circuit receives. Unlike in somata and dendrites, axonal recording of neural activity--both electrically and optically--has been difficult to achieve, thus preventing comprehensive understanding of neuronal circuit function. Here, we developed an active transportation strategy to enrich GCaMP6, a genetically encoded calcium indicator (GECI), uniformly in axons with sufficient brightness, signal-to-noise ratio, and photostability to allow robust, structure-specific imaging of pre-synaptic activity in awake mice. Axon-targeted GCaMP6 (axon-GCaMP6) enables frame-to-frame correlation for motion correction in axons and permits subcellular-resolution recording of axonal activity in previously inaccessible deep brain areas. We used axon-GCaMP6 to record layer-specific local afferents without contamination from somata and intermingled dendrites in the cortex. We expect axon-GCaMP6 will facilitate new applications in investigating afferent signals relayed by genetically defined neuronal populations within and across specific brain regions.

To whom correspondence should be addressed: lintian@ucdavis.edu and leopoldo.petreanu@neuro.fchampalimaud.org.

Author contributions

L.P. and L.T initiated the project; G.B. and L.T. designed the projects, developed axon-targeted GCaMP6, performed characterization of ADR, photostability and SNR in vitro in dissociated neuronal culture and performed histological characterization of ADR and expression in vivo. Y.L. G.M., and N.J. performed in vivo characterization of dLGN axons in V1, deep-brain imaging, and layer-specific cortical axonal recording in V1. M.F and L.P. performed in vivo characterization of L1 axons in V1 projected from LP and area LM and examined frame-to-frame correlation. G.B. analyzed data from in vivo imaging with help from Y.L., M.F., and G.M., E.U. performed viral injection. G.B. and L.T. wrote the manuscript with critical input from all authors.

Competing financial interests

The authors declare no competing financial interests.

Introduction

Neural circuits consist of large populations of cell bodies connected by axons and dendrites. Understanding circuit computations (and even those of single neurons) requires knowing the neural representation carried by inputs, local neurons and outputs that lead to input-output transformations. Axons are very thin (typically less than 1μm in diameter), branch numerous times, can vary in length, and travel the full extent of the brain, thus making activity recording difficult. Microelectrode-based recording methods do not allow for the isolation of single axons and lack the genetic specificity required to identify the source of the recorded input signals. Genetically encoded calcium indicators (GECIs; for review, see [1]), such as the GCaMP family[2,3,4,5], have enabled recordings from the somata and dendrites of genetically defined neuronal populations in behaving animals. However, optical recording from individual axons and presynaptic structures with GECIs is suboptimal, thus limiting comprehensive interrogation of afferent inputs.

Untargeted GCaMPs (u-GCaMPs) preferentially label somatodendritic compartments and diffuse poorly to distal axons. Low expression levels of GECIs in pre-synaptic structures make even visualization of axons with expression difficult, and functional imaging of dimly labeled axons produces poor signal-to-noise ratio (SNR), particularly deep in tissue where light scattering requires a high photon budget. Consequently, axonal GECI imaging is typically performed only under near-ideal conditions, such as shallow terminal fields of relatively short projections[6,7,8–10,11,12–14]. Even so, low SNR and contamination from intermingled dendritic arbors closer to the expression source degrades imaging quality and complicates assignment of fluorescence to specific axons due to overlapping dendritic signal. Presynaptically-targeted GCaMPs have been developed[15], but suffer substantially from photobleaching[16] due to restricted diffusion in the excitation volume. We thus developed an approach for axonal GCaMP imaging that offers greater enrichment and photostability than previous techniques.

Results

Engineering and characterization of an axon-enriched GCaMP

To design a high-efficacy axon-enriched GCaMP6, we screened a panel of targeting motifs that have been previously reported to drive axonal localization (Supplementary Fig. 1a). We chose eight motifs with diverse targeting mechanisms and fused them to either the N- or C-terminus of GCaMP6m. These motifs included: the 20 residue dipalmitoylation domain found at the n-terminus of growth-associated protein-43 (GAP43)[17], the 15 residue c-terminus of the amyloid precursor protein (c-APP)[18], the ankyrinB binding motif (ABM) derived from the N and P/Q type voltage dependent calcium channels[19], the mRNA localization zipcode found within the 3’ untranslated region of the tau protein[20], the 26 residue tandem palmitoylation and myristoylation domains found at the n-terminus of the Src tyrosine kinase, Lck[21,22], the synthetic myosin VI binding domain (MVIBD) derived from peptides found in Optineurin and Disabled homolog 2[23], the 20 residue palmitoylation domain found at the c-terminus of Paralemmin[24], and finally the full-length synaptophysin, which was previously reported to target GCaMP effectively to axons[15], but also rapidly photobleaches during in vivo imaging[16] (Fig. 1a **and** Supplementary Fig. 1a).

We first characterized the expression pattern of each construct in dissociated rat hippocampal neuronal culture. We measured a normalized axon-to-dendrite ratio (nADR)[25] to determine the extent to which each probe localized to axonal and somatodendritic compartments relative to a co-expressed, untargeted red fluorophore (mRuby2) (Fig. 1 b-c **and** Supplementary Fig. 1b). The 20 residue dipalmitoylation domain derived from the N-terminus of GAP43 drove the highest enrichment of GCaMP6m in axons (Fig. 1b, Supplementary Fig. 1b), with ~5-fold increased nADR compared to u-GCaMP6m (nADR of GAP43-GCaMP6m: 4.83±0.78, nADR of u-GCaMP6m: 0.76±0.08, P = 3.09E-5) (Fig 1c). The GAP43 motif also targeted GCaMP6s and GCaMP6f to axons with equally increased nADR with GCaMP6m (nADR of GAP43-GCaMP6s: 5.65±1.03, nADR of GAP43-GCaMP6f: 4.58±0.44, P = 8.72E-5 and 2.19E-6, respectively). In contrast, direct tethering to a presynaptic protein (i.e., synaptophysin-GCaMP[15] (syGCaMP)) as previously reported only moderately targeted the probe to axons, about a 2-fold increase compared to u-GCaMP6m (nADR: 1.70±0.11, P = 0.23). The GAP43-fused GCaMP6m showed rapid enrichment in axons as early as two days post-transfection, remained stable across 5 days (Supplementary Fig. 1c), and displayed more consistent labeling across axonal arbors than u-GCaMP6m or syGCaMP6m (Supplementary Fig. 1d, e). We refer to GAP43-fused GCaMP6 as axon-GCaMP6 and further characterized it in vivo.

We next sought to determine the targeting efficiency of axon-GCaMP6 in long-range axons in vivo. We engineered bicistronic constructs encoding either axon-GCaMP6s or u-GCaMP6s followed by a P2A peptide-fused untargeted red fluorophore (mRuby3)[26] such that red fluorescence allowed normalization of expression levels (Fig. 1d). We labeled neurons in dorsal lateral geniculate nucleus of the thalamus (dLGN) with recombinant adeno associated virus (rAAV) encoding axon-GCaMP6s-P2A-mRuby3 or u-GCaMP6s-P2A-mRuby3. We achieved similar patterns and levels of transduction of red fluorescence using both viruses (Supplementary Fig. 2 **and** 3). Strikingly, in animals injected with axon-GCaMP6s-P2A-mRuby3, we found that somata and dendritic arbors of dLGN neurons were essentially devoid of green fluorescence after 2-weeks of expression, while the axons of this cell population were brightly labeled in V1 (Fig. 1e). To calculate nADR, we calculated the ratio of green fluorescence from dLGN axons in layer 4 (L4), the primary target of the dLGN axons within V1, to those from somata within dLGN, and normalized to the ratio of red fluorescence. Similar to what we observed in dissociated neuronal culture, axon-GCaMP6s displayed about ~5-fold increase to nADR over u-GCaMP6s (axon-GCaMP6s: 2.54±0.28; u-GCaMP6s: 0.50±0.06; P = 4.37E-16)(Fig. 1f). These data suggested that axon-GCaMP6s was actively transported into distal axons.

We then sought to characterize the photostability and diffusibility of axon-GCaMP6m using Fluorescence Loss in Photobleaching (FLIP) and Fluorescence Recovery After Photobleaching (FRAP) assays (Fig. 2a, d; Supplementary Fig. 4a-e). Axon-GCaMP6m diffuses rapidly between adjacent axonal compartments at a rate similar to u-GCaMP6m (mobile fraction of axon-GCaMP6m: 0.77±0.02; mobile fraction for u-GCaMP6m: 0.90±0.03) (Fig. 2b, c **and** Supplementary Fig. 4d, e). High diffusibility led to fast replenishment of bleached molecules, thus greatly reducing effective photobleaching of axon-GCaMP6m (Fig. 2e). In contrast, syGCaMP6m displayed significantly reduced

diffusibility, resulting in rapid photobleaching consistent with previous in vivo observations[16] (mobile fraction for syGCaMP6m: 0.28±0.01) (Fig. 2c, e **and** Supplementary Fig. 4c). Additionally, the dipalitoylation modification of axon-GCaMP6m provided better photostability than some of the other targeting motifs that either contained myristoylation domains (e.g., Lck) or multiple binding sites for transport effectors (e.g., MVIBD), which is consistent with previously reported results[27] (Supplementary Fig. 4c).

To confirm that axon-GCaMP is more photostable in vivo, we labeled dLGN with rAAV encoding u-GCaMP6s, syGCaMP6s, or axon-GCaMP6s (Fig. 2f) followed by continuous two-photon excitation through a cranial window in awake, behaving animals. Upon hundreds of seconds of illumination, the fluorescence of dLGN projections in superficial V1 labeled with either u-GCaMP6s or axon-GCaMP6s largely remain unchanged (Fig. 2g, Supplementary Fig. 4f). In contrast, the fluorescence signals of syGCaMP6s labeled projections decreased by more than 50% during the initial 400 seconds of illumination (Fig. 2g, Supplementary Fig. 4f).

Finally, we characterized the sensitivity of axon-GCaMP6 in response to field potential stimuli. We transfected axon-GCaMP6s-P2A-mRuby3 or u-GCaMP6s-P2A-mRuby3 into cultured hippocampal neurons. After five days of expression in dissociated neuronal culture, the ratio of green-to-red fluorescence of axons expressing axon-GCaMP6s was about 5-fold higher than those labeled with u-GCaMP6s (axon-GCaMP6s: 0.100, u-GCaMP6s: 0.023) (Fig. 2h **and** Supplementary Fig. 5a). In response to a variety of field potential stimuli (30Hz), fluorescence changes ($\Delta F/F_0$) of axon-GCaMP6s were similar to u-GCaMP6s, with higher basal fluorescence levels (Supplementary Fig. 5b) and lower noise, resulting in ~2-fold enhancement in SNR (for details, see Methods) across all stimuli (Fig. 2i, j, Supplementary Fig. 5b). Kinetics (Supplementary Fig. 5c, d), size of detected regions of interest (ROIs, ~0.5-10um^2) [28] (Supplementary Fig. 5e, f), and fluorescence brightness from the secondary fluorophore, mRuby3 (Supplementary Fig 5g, h), were similar between axon-GCaMP6s and u-GCaMP6s. We therefore conclude that increased probe enrichment in axons was the primary driver of the observed enhancement to SNR displayed by axon-GCaMP6s.

In vivo imaging of distal afferent calcium signals with axon-GCaMPs

We sought to determine whether improved properties of axon-GCaMP6 could enable in vivo applications that are difficult with u-GCaMP. Thalamocortical projections to sensory cortices, such as those projected from dLGN and lateral posterior nucleus of the thalamus (LP), are dimly labeled by u-GCaMPs[9,11,12]. To determine the effect of axonal enrichment on SNR, we imaged the response to drifting gratings of dLGN (Fig. 3a-e, Supplementary Fig. 6a-c) and LP (Fig. 3f-j, Supplementary Fig. 6d-f) cells at their axon terminals in layer 1 (L1) of V1.

We successfully recorded calcium signals in thalamocortical axons in superficial layer of V1 in response to drifting grating stimuli[11,12] (Fig. 3c, h). Axons labeled with axon-GCaMP6s displayed a ~7-fold increase in normalized basal green fluorescence over u-GCaMP6s for dLGN axons (5.86 (axon-GCAMP6s), 0.85 (u-GCaMP6s); P = 2.15E-259). LP axons similarly showed an ~4-fold increase (19.47 (axon-GCaMP6s), 5.08 (u-GCaMP6s); P =

1.24e-319) (Fig. 3b, e, g, j and Supplementary movie 1). While u-GCamP6s expressing axons displayed bright fluorescent varicosities that are likely boutons [6,7,29], axon-GCaMP6s fluorescence was relatively homogenous in both axonal shafts and varicosities (Fig. 3b, g). Because signal amplitude is generally lower in the axonal shaft than in varicose structures (Supplementary Fig. 7, see also [29]), we drew ROIs over varicosities (for details, see Methods) and measured visual responses of thalamocortical axonal populations. SNR (for details, see Methods) of axon-GCaMP6s in response to drifting gratings was significantly improved for dLGN axons (2.73 (axon-GCAMP6s), 1.54 (u-GCaMP6s); P = 9.56E-130) as well as LP axons (1.57 (axon-GCaMP6s), 0.98 (u-GCaMP6s); P = 1.13E-95) (Fig. 3d, e, i, j). Consistent with our dissociated neuronal culture data, a similar $\Delta F/F_0$ was observed across both constructs for dLGN axons (0.72 (axon-GCAMP6s), 0.40 (u-GCaMP6s); P = 5.41E-73) and LP axons (0.86 (axon-GCaMP6s), 0.83 (u-GCaMP6s); P = 0.44) (Supplementary Fig. 6b, c, e, f).

We next compared the sensitivity of axon-GCaMP6s with syGCaMP6s. Because syGCaMP6s bleaches more rapidly than other GCaMP6s designs (Supplementary Fig. 4f, Supplementary Fig. 8 a-c), we observed trial number-dependent rundown of ΔF/F and SNR (Supplementary Fig. 8 c-e). We then compared the brightness of ROIs only in the first 25 seconds of imaging. At this early period of the imaging session, brightness of axon-GCaMP6s was less than 2-fold higher than syGCaMP6s (5.57 (axon-GCaMP6s), 3.45 (syGCaMP6s); P = 3.13E-19) (Supplementary Fig. 8 f, g). When averaged across all trials, syGCaMP6s exhibited comparable ΔF/F (0.72 (axon-GCaMP6s), 0.65 (syGCaMP6s); P = 0.016) and significantly lower SNR (2.73 (axon-GCaMP6s), 1.63 (syGCaMP6s); P = 1.14E-25) than axon-GCaMP6s (Supplementary Fig. 8 h-k).

In addition, we examined axonal enrichment and SNR of GCaMP6f when fused to the GAP43 targeting motif. As expected, we observed 9-fold increase in normalized basal green fluorescence (5.99 (axon-GCaMP6f), 0.60 (u-GCaMP6f); P = 9.87E-98) and 1.5-fold increase in SNR over u-GCaMP6f for dLGN axons(1.27 (axon-GCaMP6f), 0.78 (u-GCaMP6f); P = 1.20E-09, Kolmogorov-Smirnov test) (Supplementary Fig. 9).

We did not observe significant differences in population orientation or direction preference between axon-GCaMP6s and u-GCaMP6s labeled thalamocortical axons (Supplementary Fig. 10 a-f). Further, the kinetics of responses were not perturbed beyond what would be expected for higher levels of GCaMP indicator expression [30] (Supplementary Fig. 10 g-i). Together, these data suggest that axon-GCaMP6s expression did not alter neuronal physiology. Our data thus show that axon-GCaMP6s enriches in long-range axons resulting in enhanced SNR in vivo without interfering with circuit properties.

Axon-GCaMP6 can also be efficiently expressed in short, cortico-cortical projections at early time points following viral induction when u-GCaMP is only minimally expressed (Supplementary Fig. 11a). Two weeks after injection of u-GCaMP6s or axon-GCaMP6s virus into lateromedial (LM) visual cortex, we observed minimal expression of u-GCaMP6s in LM axons in V1 and only 20% of analyzed ROIs were visually responsive. In contrast, axon-GCaMP6s enriched in axons displaying bright axonal and bouton labeling with 80% of axons responding to visual stimuli. The SNR was increased 3-fold (1.09 (axon-GCaMP6s),

0.35 (u-GCaMP6s); P = 5.62E-12), while $\Delta F/F_0$ showed a 2-fold improvement (0.65 (axon-GCaMP6s), 0.30 (u-GCaMP6s); P = 1.06E-07) (Supplementary Fig. 11), suggesting active transportation of axon-GCaMP6 allows imaging at earlier time points in axons.

The enhanced brightness and photostability offered by axon-GCaMP6 now permits robust cross correlation-based correction of motion artifact in axonal structures (Fig. 3k, l, m). Motion artifacts plague imaging experiments in awake, behaving animals, but are usually correctable (at least in part) with brightly labeled cell bodies. Image registration in axons is especially challenging if the axons are only dimly labeled, particularly as axons are tiny and can easily move within the imaging plane. These difficulties are especially pronounced at commonly used acquisition speeds, which leads to limited photon budget and poorly defined structural information for performing motion correction. As such, axonal motion artifacts are frequently uncorrectable. The increased brightness and photostability of axon-GCaMP6s at distal axons (Fig. 3b, e, g, j; Supplementary Fig. 11 b, f) greatly increases frame-to-frame correlations relative to u-GCaMP6s (5-10 fold) (correlations normalized to u-GCaMP6s, dLGN axons: 4.83; LP axons: 4.76; LM axons: 10.41) (Fig. 3k, l, m; Supplementary Fig. 11e), allowing efficient motion artifact correction in axonal structures[31].

Axon-GCaMP enables imaging of thalamic boutons in deep cortical layers in vivo

The small size and dim fluorescence of axons and boutons similarly presents difficulties for imaging deep structures, such as in the subgranular layers of cortex. Even with adaptive optics, tuning properties of thalamic axons are difficult to obtain more than 400 μm below the pia using u-GCaMP6s[11]. As a comparison, boutons of axons projecting from dLGN to the supra- and subgranular layers of V1 were imaged with u-GCaMP6s and axon-GCaMP6s in head-fixed, awake mice. Average fluorescence intensity was recorded in 100 μm bins down to 500 μm, and normalized to the square of the excitation laser power (Fig. 4a, b). Axon-GCaMP6s was brighter (Fig. 4b) while providing better contrast (Supplementary Fig. 12) than u-GCaMP6s at all depths. This enhanced brightness facilitated the first recordings of dLGN L5/6 axons at depths down to 600μm (Fig. 4c, d, e). Orientation-specific fluorescence transients ($\Delta F/F_0$) were clearly observable and from these transients, we calculated orientation tuning curves of these deep cortical axons (Fig. 4c, d, e). Similarly, axon-GCaMP6f was also brighter at all depths than u-GCaMP6f. Especially at 600 μm, axon-GCaMP6f allowed for effective recordings of orientation-specific tuning, whereas no fluorescence signal sources were observable with u-GCaMP6f (Supplementary Fig. 13). Thus, axon-GCaMP6 allows in vivo interrogation of previously inaccessible axons deep within tissue.

Axon-GCaMP enables layer-specific imaging of local afferents in vivo

Lastly, we utilized a cre-dependent axon-GCaMP6 to record orientation and direction tuning of axons projecting from L4 V1 neurons in each recipient cortical layer without contamination of signal from somato-dendritic sources (Fig. 5). L4 excitatory neurons were labeled in *Scnn1a*-Tg3-Cre mice using rAAV encoding FLEx-axon-GCaMP6s-P2A-mRuby3 or FLEx-GCaMP6s-P2A-mRuby3 driven by the human *synapsin1* promoter (Fig. 5a, b). Three weeks after infection, we observed L4 axons labeled with axon-GCaMP6s ramifying across all cortical layers, whereas u-GCaMP6s primarily labeled the somato-dendritic

compartments of L4 neurons (Fig. 5c). L4 axons and boutons were easily identifiable from intermingled dendritic structures within different cortical layers (Fig. 5c). The average green-to-red ratio of axon-GCaMP6s in axons was about 5-fold higher than that of u-GCaMP6s (axon-GCaMP6s: 2.25, u-GCaMP6s: 0.53; P < 4.94E-324) (Fig. 5d). In contrast, the green-to-red ratio of axon-GCaMP6s in dendrites was 6-fold lower compared to u-GCaMP6s, indicating specific axonal enrichment of axon-GCaMP6s (axon-GCaMP6s: 0.21, u-GCaMP6s: 1.24; P = 1.57E-26) (Fig. 5e).

In agreement with our histological results, no dendritic structures were observed in the in vivo 2-photon fields of view (Fig. 5f **and** Supplementary Fig. 14a). In contrast, animals transduced by u-GCaMP6 showed numerous intermingled dendritic structures (Supplementary Fig. 14b). Using axon-GCaMP6s, we were able to readily detect the response (Fig. 5g-i) and calculate the orientation tuning properties of individual boutons from L4 neurons throughout their projection fields across cortical depths to 600 μm (Fig. 5i, Supplementary Fig. 15).

In addition, axon-GCaMP6s permits layer-specific output recording of axons projected from other cortical layers as well. When rAAV-hSynapsin-FLEx-axon-GCaMP6s was introduced to V1 of *Rbp4*-Cre or *Ntsr1*-Cre driver mouse lines to restrict expression to L5 or L6, respectively, single-bouton tuning properties were clearly detectable in their recipient layers (Supplementary Fig. 14). Thus, axon-GCaMP6s permits recordings of local afferents down to individual boutons even when dendritic structures of transduced cells are present within the same tissue volume.

Discussion

We have overcome the limitations of genetically encoded calcium indicators to allow robust imaging of afferent calcium transients deep in tissue, with structural specificity and with greater SNR. We achieved this by creating an axon-targeted GECI, axon-GCaMP6, which enriches exclusively in local or distal axons with enhanced brightness and photostability, thus expanding calcium imaging beyond the soma and dendrites. Although presynaptic-targeted GCaMPs, such as SyGCaMP6, have been developed, imaging with sensors that localize tightly to pre-synaptic compartments suffers substantially from photobleaching (Fig. 2g). In contrast, axon-GCaMP6 is diffusible, photostable, and displays enhanced SNR. The enrichment of axon-GCaMP6 in axons offers enhanced frame-to-frame cross-correlation without extensive averaging, which greatly facilitates motion correction of axons in vivo.

Axon-GCaMPs enable new applications of calcium imaging with subcellular resolution in deep cortical layers non-invasively. Thalamic axons ramify in both supra- and subgranular layers. However, in vivo calcium imaging of thalamic boutons has been limited to superficial layers (<400 μm below pia) with untargeted GCaMP6s or GCaMP6f even with the aid of adaptive optics. With axon-GCaMP6s and axon-GCaMP6f, the tuning properties of individual thalamocortical boutons in subgranular layers now can be readily imaged without the aid of adaptive optics while preserving good SNR, which will open the door for new studies of long-range communication in deeper tissue. As an example application, it is now established that infragranular layers including L5[32,33] and L6[34] receive direct

thalamocortical innervation from primary thalamic nuclei. Previous methods have left axons which forms these connections functionally inaccessible. Deeper imaging made possible by axon-GCaMP6 will alleviate this methodological gap.

Finally, we utilized axon-GCaMP6 to record orientation and direction tuning of layer-specific axonal inputs projected from local neurons while excluding signal from their extensively intermingled dendritic structures. Recording from local axonal inputs with layer specificity remains difficult largely due to contamination from intermingled dendritic structures. Generally, it remains unclear what information is provided by local afferents on a layer by layer basis. Axon-GCaMP6 allows direct interrogation of these signals with requisite spatial resolution while avoiding contaminating signal from transduced dendrites.

Long-term, high-level expression of GECIs in the mouse brain can result in prolonged response or nonfunctional indicators and perturb circuit function. In the case of axon-GCaMP6, the enrichment in axons did not perturb neuronal physiology as evidenced by similar kinetics and properties of orientation tuning to those of untargeted GCaMP6 after long-term expression (4-6 weeks). Although we did not observe adverse effects in our experiments, physiological impact should be carefully examined in each experimental preparation. Possible interference with synaptic physiology should also be examined.

Axon-GCaMP will be useful in a number of other applications and brain regions, and the targeting tag might be transferable to other payloads. The axonal targeting sequence is only 20 amino acids, which will allow easy fusion with both red-shifted[35,36] and FRET-based GECIs[37–41] or other genetically encoded sensors of neural activity, such as neurotransmitter sensors[42]. Axonal enrichment may be particularly useful for red indicators as this approach enhances brightness in small subcellular compartments without extensive optimizing of basal fluorescence of the indicator itself. In addition, it may be possible to target actuators[43] to axons to allow axonal-specific activation of input signals.

Though axon-GCaMP6 is a superior tool for afferent imaging in the mammalian brain, axon-GCaMP6 is not intended as a replacement for monitoring synaptic calcium using syGCaMP. Indeed, syGCaMP indicators have proven their utility for uncovering the coupling between pre-synaptic calcium and vesicular release in both dissociated neuronal cultures[44,45] , flies[46], and larval zebrafish[47]. It has also been used to address systems-level questions in the more optically accessible larval zebrafish[48,49]. However, in mouse brain, we observed significant photobleaching of syGCaMP (Fig. 2g), which precludes imaging for longer than a few minutes. When expressed in dissociated neurons, syGCaMP displayed significantly reduced diffusibility, limiting replenishment of photobleached molecules in boutons. The fast photobleaching in vivo is therefore presumably due to slow replenishment of bleached molecules into the imaged volume during prolonged imaging experiments. As the axon-GCaMP targeting strategy maintains fast diffusibility, it is more photostable than syGCaMP6 both in vitro and in vivo.

In vivo, axon-GCaMP6 reports axonal calcium transients in both axonal shafts and putative boutons more effectively than u-GCaMP6. We also observed that fluorescence responses of axon-GCaMP6 in shafts were smaller than those in putative boutons (Supplementary Fig. 7),

consistent with previous observations that calcium signals in axons concentrated in the proximity of boutons (see also [29,50]). When combined with post-hoc structural analysis, it is possible to delineate calcium signals originating in axon shafts or putative boutons. However, when recording afferent signals from specific axons in vivo, the interest is often focused on information encoded by axonal signals. Therefore, differentiating signals at synapses versus axons does not usually add additional information for answering questions at systems level. Axon-GCaMP6 allows more effective analysis of Ca^{2+} signals within axonal shaft compartments which exhibit signals that are highly correlated with those found in boutons of the same axon [6,14]. As axonal imaging becomes a rich area of research that needs calcium indicators that are photo-stable, bright and capable of specifically reporting axonal signals, we expect this specialized GCaMP6 will greatly facilitate recordings from afferent signals of any length with subcellular resolution.

Online Methods

Protein engineering

All constructs were designed using a combination of overlap extension cloning and gBlock gene fragments (Integrated DNA Technologies). All constructs were flanked by BamHI with downstream Kozak sequence and start codons as well as HindIII for final subcloning onto pAAV-*hSynapsin1* vectors. Alternatively, constructs were flanked by SacI and AflII sites for subcloning into custom pAAV-*hSynapsin1*-FLEx vectors.

Concurrent two-color fluorophore expression was achieved by the use of either two plasmids with mRuby2 as the red reference fluorophore or a bicistronic approach in which the GCaMP construct was separated by a P2A sequence[1] from a downstream mRuby3. The two-plasmid approach was used for all in vitro characterization while the bicistronic approach was used for *in vivo* characterization. Functional assays were performed with no reference fluorophore.

Dissociated hippocampal neuronal culture

For ADR and diffusion analyses, primary hippocampal neuronal cultures were prepared as described previously[2]. Briefly, P0 or E18 pups were decapitated, and the brains were dissected into ice-cold neural dissection solution (NDS, 10 mM HEPES (Sigma) in Hank's Balanced Salt Solution (HBSS, Thermo Fisher Scientific), pH 7.4). Hippocampi were removed, enzymatically digested with papain (~60 units), washed with pre-warmed plating medium (PM, Minimal Essential Medium (Thermo Fisher Scientific) supplemented by 10% fetal bovine serum (Thermo Fisher Scientific) and 100U/mL Penicillin-Streptomycin (Thermo-Fisher Scientific)) and then mechanically digested by trituration. Cells were plated on 35mm MatTek glass bottom dishes (MatTek) coated with Matrigel matrix (BD Biosciences) or a mixture of poly-L-ornithine (Sigma-Aldrich) and laminin (Sigma-Aldrich), and kept at 37 °C, 5% CO_2 in PM for ~24 h and then in Neurobasal medium (Thermo Fisher Scientific) supplemented by 10% B27 (Thermo Fisher Scientific) for the experiment duration with half medium exchanges every 4 days. On the fifth day in vitro (DIV), cells used for ADR and FRAP/FLIP experiments were transfected by Effectene (Qiagen) following the manufacturer's recommendation with the following modification: for

100μL transfection complex, we included only 5μL Effectene reagent. Such cells were subsequently used for imaging experiments between 2 and 5 days post-transfection. Cells used for SNR analysis were transduced on DIV5 by *rAAV-hSynapsin-GCaMP6s-P2A-mRuby3-WPRE-SV40* or *rAAV-hSyanspin-axon-GCaMP6s-P2A-mRuby3-WPRE-SV40* to drive near-complete transduction of all cultured neurons. All cultures were imaged on a laser scanning confocal microscope (Zeiss 710) equipped with 405, 488, 514, 561, and 633 laser lines. Band limits for detection of GCaMP fluorescence were set between 493 and 541nm while collection of mRuby fluorescence was beyond 590nm. Prior to imaging, cultures were washed and incubated in HBSS containing 2mM $MgCl_2$ and $CaCl_2$ to minimize background due to fluorescent culture medium components. For experiments requiring field stimulation, an RC-37FS perfusion insert (Warner Instruments) was fitted into the MatTek. During such experiments, spontaneous network activity was suppressed by inclusion of 20μM of 6-cyano-7-nitroquinoxaline-2,3-dione (CNQX) and 40μM of D-(−)-2-Amino-5-phosphopentanoic acid (D-APV) to the imaging medium. All data collected for quantitative comparisons was collected with identical imaging parameters with the exception that the laser power was adjusted to just below saturation for the imaged cell or fields' brightest feature.

Quantification of axon to dendrite ratio

Calculation of the normalized ratio was performed following the method of Lewis et al[3]. Specifically, an un-normalized ratio of fluorescence between the axon and somatodendritic compartments was calculated as:

$$uADR = \frac{F_{TestFP,Axon}}{F_{TestFP,Somatodendritic}}$$

where F_{TestFP} refers to the background-subtracted average fluorescence of GCaMP within the indicated structure. This measure was then normalized to similar values for mRuby2 as:

$$nADR = \frac{uADR}{\left(\frac{F_{RefFP,Axon}}{F_{RefFP,Somatodendritic}}\right)}$$

where F_{RefFP} refers to the background-subtracted average fluorescence of mRuby2 within the indicated structure. Normalizing to the distribution of red fluorescence thus controls for differences in diffusivity across different cells.

Fluorescence loss in photobleaching and fluorescence recovery after photobleaching

For FLIP experiments, axonal segments greater than 100 μm from the soma were targeted for imaging. After a baseline of 10 images, images were acquired alternating with application of bleaching pulses over a 10 μm circle centered in the imaged frame. The same 488 nm line from a 25 mW Argon laser was used as the bleaching excitation with a pixel dwell time of 1.58 μs. Loss of fluorescence was then tracked within a background-subtracted region of interest covering the axon within the bleached circle. For these experiments, all fields of view included an axon that was not directly attached to the bleached segment.

Fluorescence within this control axon segment was monitored to ensure that imaging did not cause greater than a 5% decrease in baseline fluorescence. Imaging sessions in which the control process fluorescence dropped by greater than this threshold were discarded.

FRAP was also performed to extract diffusion coefficients of axonal GCaMP variants[4]. Imaging and bleaching parameters were identical to those used in the FLIP experiments with the exception that a single bleaching pulse was applied. To drive sufficient bleaching, experiments were conducted in imaging medium supplemented by 5 μM of the calcium ionophore ionomycin, effectively increasing the extinction coefficient of the GCaMP[5]. Normalized post bleach profiles, $f_{Postbleach}(x)$, were determined by dividing the fluorescence profile directly following the bleaching epoch by that preceding the bleach event. Diffusion occurring between consecutive imaging acquisitions was then corrected for by fitting the effective bleach radius, r_e, and bleach depth, K, of the normalized bleach profile to the equation:

$$\hat{f}_{Postbleach}(x) = 1 - Ke^{-x^2/r_e^2}$$

FRAP curves were then determined by fitting the recovery time course, $F(t)$, to the equation:

$$\hat{F}(t) = (1-a)\left(F_0 - F_\infty\right)e^{-t/\tau_{slow}} + a\left(F_0 - F_\infty\right)e^{-t/\tau_{fast}} + F_\infty$$

where a, F_0, F_∞, τ_{slow} and τ_{fast} are free parameters corresponding to the double exponential fraction, the initial post-bleach fluorescence, the steady-state fluorescence recovery level, and the slow and fast exponential recovery rates, respectively. The time to half recovery, $t_{1/2}$, was then determined as the time point where $\hat{F}\left(t_{1/2}\right) = \frac{F_\infty - F_0}{2}$. Finally, the diffusion coefficient, D, was recovered using the nominal user selected bleach radius, r_n, with the expression:

$$D = \frac{r_e^2 + r_n^2}{8\tau_{1/2}}$$

Characterization of performance in dissociated neuronal culture

To quantify performance of GCaMP-labelled cell culture, we performed electrical field stimulation experiments in dissociated hippocampal culture. In cultures densely transduced by virus, confocal imaging was performed on intermingled fields of axons within fields of view greater than 100 μm from the nearest visible dendritic segment. Axons imaged for this study were first masked using the mRuby3 fluorescence signal. These masks were segmented using ICY plugin split ROI[6] into ROIs with normal distribution and mean size around that of typical ROIs used in in vivo imaging experiments (0.8-10μm^2). Time-lapse calcium imaging stacks were acquired from these axons based on the GCaMP fluorescence

signal. After a 5 second baseline, 1, 2, 5, 10, 20, 40, or 80 field potentials were applied at 1V, 1ms square wave pulse at 30Hz under the control of Ephus software[7]. mRuby3-based ROIs were then analyzed with the average of the baseline period, F_0, used to calculate the fluorescent transients $\Delta F/F_0$, as $\Delta F/F_0 = (F - F_0)/F_0$. SNR was then calculated as the maximum $\Delta F/F_0$ divided by the standard deviation of the baseline period.

Animal procedures

All animal procedures were conducted according to the Portuguese Direcção Geral de Veterinária and the United States National Institutes of Health guidelines for animal research and approved by the Institutional Animal Care and Use Committee at the University of California, Davis, the Howard Hughes Medical Institute, or the Champalimaud Center for the Unknown. Wild-type mice were used for in vivo functional imaging of visual thalamic axons as well as LM cortico-cortical projections (older than P60, C57BL/6J). *Scnn1a*-Tg3-Cre mice (Jax no. 009613), *Rbp4*-Cre mice (MMRRC no. 031125-UCD), and *Ntsr1*-Cre mice (MMRRC no. 030648-UCD) of both sexes (older than P60) were used for in vivo functional imaging of cortical afferents from L4, L5, and L6 neurons, respectively. Sample sizes (number of mice, cells and/or boutons) for each experiment are stated in main text.

Viral injections

Injection procedures were essentially identical to those described in [8,9] with a few exceptions. Briefly, virus injection was performed using a glass pipette beveled at 45° with a 15-20-μm opening and back-filled with mineral oil. A fitted plunger controlled by a hydraulic manipulator (Narashige, MO10 or World Precision Instruments, UMP3) was inserted into the pipette and used to load and inject the viral solution.

For confirmation of enhanced axonal expression of axon-GCaMP6s in living mice, ~20-40 nL of *rAAV2/1-hSynapsin1-GCaMP6s-P2A-mRuby3-WPRE-SV40* (~2 × 10^{13} viral genome (vg) per mL) or *rAAV2/1-hSynapsin1-axon-GCaMP6sP2A-mRuby3-WPRE-SV40* (~3.2 × 10^{13} vg per mL) was slowly injected into dLGN (2.1 mm posterior to Bregma; 2.3 mm lateral from midline; 2.5 mm below pia). For axon-specific labeling of local cortical connections in V1, ~20-40nL of *rAAV2/1-hSynapsin1-axon-GCaMP6s-WPRE-SV40* (~1.2 × 10^{13} vg per mL) was injected to cortical L4 (*Scnn1a*-Tg3-Cre mice: three injection sites in left hemisphere centered at 3.4 mm posterior to Bregma; 2.7 mm lateral from midline; 0.3 mm below pia; injection sites are ~250 μm apart). Additionally, we produced these viruses under a 2/5 serotype to test differences in transduction efficiency. We did not find apparent differences across serotypes (data not shown).

For calcium imaging of thalamocortical and LM cortico-cortical projections, ~20-80 nL of *rAAV2/1-hSynapsin1-GCaMP6s-WPRE-SV40* (~2-4 × 10^{13} infectious units per ml) or *rAAV2/1-hSynapsin1-axon-GCaMP6s-WPRE-SV40* solution (~4 × 10^{13} infectious units per ml) was slowly injected into dLGN, LP (1.9 mm posterior to Bregma; 1.4 mm lateral from midline; 2.7 mm below Bregma), or LM (coordinates determined by intrinsic optical imaging[10,11]). For imaging of cortical neurons and local axon projections ~20-40 nl of *rAAV1-hSynapsin1-FLEx-GCaMP6s-WPRE-SV40* (~2.4 × 10^{13} infectious units per ml) or *rAAV1-hSynapsin1-FLEx-axon-GCaMP6s-WPRE-SV40* (~3.1 × 10^{12}) was injected per

injection site into V1 for cortical L4 (*Scnn1a*-Tg3-Cre mice), cortical L5 (*Rbp4*-Cre mice), or cortical L6 (*Ntsr1*-Cre mice) (three injection sites in left hemisphere centered at 3.4 mm posterior to Bregma; 2.7 mm lateral from midline; 0.4 mm below pia; injection sites were ~250 μm apart) somatic or local cortical axon imaging, respectively. All calcium imaging data of u-GCaMP6^{+} dLGN axons was first reported by Sun and co-workers[8].

Head plate/cranial window implantation

Craniotomy and head plate implantation were carried out at the same time as virus injection for calcium imaging experiments. A 2.5-4 mm diameter craniotomy was made over the left V1 (center: 3.4 mm posterior to Bregma; 2.7 mm lateral from midline) of the anaesthetized mice with dura left intact. For experiments using adaptive optical correction of aberration, 2 μL of red fluorescent bead solution (2-μm diameter; 1:500 in saline; Life Technologies, F-8826) was deposited on the dura surface. A glass window made of either a single coverslip (Fisher Scientific no. 1.5) or two coverslips bonded with ultraviolet cured optical adhesives (Norland Optical Adhesives 61) was embedded in the craniotomy and sealed in place with cyanoacrylate. A titanium head-post was attached to the skull with cyanoacrylate glue and dental acrylic.

Visual stimulation

Visual stimuli were presented on a screen 13-17 cm distant at an angle of ~40° relative to the long axis of the animal on the contralateral side of imaged V1. The stimuli were composed of square gratings with 100% contrast, 0.04-0.07 cycles per degree, drifting at 26 degrees per second, yielding a temporal frequency of ~2Hz. For all projections, this stimulus was presented at 8 or 12 different orientations in a pseudorandom sequence. For dLGN recordings, stimuli were 12 s each, during which time the stimulus was static for the first and last 3 s, and drifting during the middle 6 s. For LP and LM recordings, baseline recordings were acquired for 2 s during which time a gray screen of mean intensity was presented, followed by a drifting grating for 2 s, and finally ending with 2 s presentation of the gray screen. A total of ten trials were presented for each stimulus orientation in the dLGN and LP recordings and twenty trials were per orientation were presented for LM recordings.

Two-photon imaging

Imaging was performed with two-photon fluorescence microscopes 2-4 weeks after virus injection, when most neurons in dLGN, LP, and cortex exhibited nuclear-excluded expression[5] of GCaMP6s. Recording from LM axons were done 14-16 days after viral injection. For dLGN recordings, mice were head-fixed, awake, and restrained. LP and LM recordings were taken in animals lightly anesthetized with 1% isoflurane and an intramuscular injection of chlorprothexene at 1 mg/kg during the imaging period. When imaging awake animals, mice were habituated to experimental handling by being head-fixed onto the sample stage with its body restrained under a half-cylindrical cover 1 week after surgery. This procedure was repeated 3-4 times for each animal, and each time for 15-60 min. Each experimental session lasted between 45 min to 3 h. Multiple sections were imaged within the same mouse. GCaMP6 was excited at 900-940nm with a Ti:Sapphire laser (Ultra II, Coherent) or an optical parametric oscillator (InSight DeepSee, Spectra-physics) that was focused by either a Nikon 16×, 0.8 NA or an Olympus 25×, 1.05 NA

objective. Emitted fluorescence photons were detected by a photomultiplier tube (H7422PA-40, Hamamatsu).

Axonal images from the brain surface down to up to 600 μm below pia were acquired using custom LabVIEW software or ScanImage5[7]. Images of thalamocortical can cortico-cortical axons in L1 were taken from 0-80 μm below the pia. For comparison of depth characteristics of u-GCaMP6s and axon-GCaMP6s, imaging fields were binned at 100 μm intervals down to a depth of 450 μm. All imaging areas were confirmed to be in V1 by stereotactic coordinates (3.4 ± 0.6 mm posterior to Bregma and 2.7 ± 0.6 mm lateral from midline) or intrinsic signal imaging. Typical images for dLGN and V1 axons had 256 × 256 pixels, at 0.3 μm per pixel and ~2-3 Hz frame rate. Typical images of LP and LM axons were acquired at 512 × 512 pixels, at 0.3-0.35 μm per pixel with a ~15 Hz frame rate.

Fixed tissue preparation

Following viral injection at time points specified within the main text, mice were deeply anaesthetized with isoflurane and transcardially perfused with PBS and then 4% paraformaldehyde (wt/vol). Brains were removed and post fixed overnight in paraformaldehyde. Coronal brain slices were cut to 30-60 μm thickness using a vibratome (V1200S, Leica) or cryostat (CM1860, Leica). Fluorescence images of these sectioned brains were acquired on a laser scanning confocal microscope (Zeiss LSM 710) equipped with 405-, 488-, 514-, 561, and 633-nm excitation laser lines. Images were collected using the following Plan-Apochromat objectives: 10×/0.45 NA (optical section step of 2 μm), 20×/0.8 NA (optical section step of 1.0 μm), 40×/1.3 NA oil immersion (optical section step of 0.5 μm), and 63×/1.4 NA oil immersion (optical section step of 0.5 μm). For all calculations of ADR, images were first acquired in the somatic field with laser power set at a level just below saturation of all features in each channel. These same settings were applied during image acquisition in the axonal fields. nADR was then calculated as described in *Quantification of dendrite to axon ratio* with somata from an entire slice used as the somatic component and layer 4 axonal projections used as the axonal component.

In vivo image analysis

Lateral motion artifact in 2-photon imaging stacks was corrected using a cross-correlation based registration algorithm[12] where cross-correlation was used to determine translational shifts in images. In each image stack, the mean projection was used as the registration reference. Several rounds of registration and re-averaging of the stack were performed to decrease $\sum_k \left(\Delta x_k^2 + \Delta y_k^2\right)$, where Δx_k and Δy_k represent the horizontal and vertical shifts of the kth image, respectively. This process was repeated once for LP and LM data and for up to 7 iterations for the dLGN[8] data.

ROI selection:

In average or standard deviation images of registered image stacks, labeled axons appeared as bright spots in u-GCaMP6 and as filled axonal shafts and varicosities in axon-GCaMP6. For analysis of both u-GCaMP6 and axon-GCaMP6 experiments, circular ROIs (0.8-4μm^2) were manually drawn over varicosities that likely correspond to presynaptic boutons[9,13].

Characterizing ΔF/F and SNR in vivo:

For stacks derived from LP and LM axons, F_0 was calculated as the average of the baseline fluorescence for each stimulus presentation. For dLGN axons, the mode of the fluorescence intensity histogram from each ROI was used as F_0. Fluorescence transients were then calculated as $\Delta F/F_0 = (F - F_0)/F_0$. Averaged $\Delta F/F_0$ traces were then derived from the mean across ten trials of the same orientation. Resultant traces were then averaged over the period of stimulus presentation to derive a $\Delta F/F_0$ value for each ROI. The standard deviation of the $\Delta F/F_0$ signal during the period prior to presenting the moving visual stimulus was calculated across trials and the resultant values were averaged together. SNR was calculated by dividing the $\Delta F/F_0$ value by the standard deviation.

To characterize the tuning properties of axonal boutons, we followed the previously described procedure[8]. Briefly, the response R of each ROI to a visual stimulus was defined as the average $\Delta F/F$ across the window of drifting gratings. For ROIs with significantly different responses across the drifting directions (one-way ANOVA, $P < 0.05$), we fit their normalized response tuning curves to grating drifting angle θ with a bimodal Gaussian function[14].

$$R(\theta) = R_{offset} + R_{pref} e^{-\frac{ang(\theta - \theta_{pref})^2}{2\sigma^2}} + R_{oppo} e^{-\frac{ang(\theta - \theta_{pref} + 180)^2}{2\sigma^2}}$$

Here θ_{pref} is the preferred orientation, R_{offset} is a constant offset, and R_{pref} and R_{oppo} are the responses at θ_{pref} and $\theta_{pref} - 180$ degrees, respectively. $ang(x) = \min(x, x - 360, x + 360)$ wraps angular values onto the interval 0° to 180°. For the dLGN data, only ROIs whose tuning curves were well fit by the bimodal Gaussian function were considered orientation selective. In LP and LM data, ROIs were considered visually responsive if a two-sided t-test between the fluorescence values during the baseline and stimulus period resulted in significance at an alpha value of 0.001.

For determining the frame to frame correlations, we calculated the 2-D correlation between frames of registered image stacks using the Matlab function corr2. Brightness of imaged varicosities from the dLGN thalamocortical projections was determined by normalizing pixel fluorescence value to the square of the excitation laser intensity[15]. Contrast was then determined by taking profiles across axonal structures and normalizing these profiles to the peak intensity.

Statistical methods

All statistical analyses were performed in Matlab (Mathworks) or Prism (GraphPad). We used parametric and non-parametric ANOVA, Wilcoxon's rank-sum test, and Kolmogorov-Smirnov test. All tests were two-tailed. Error bars are standard error of the mean or standard deviation as indicated in figure legends and main text. No statistical methods were used to predetermine sample size. However, sample sizes are consistent with those reported in previous publications[11,12]. The data collection was randomized in the organization of the

experimental conditions and visual stimulus presentations. Data collection and analysis were not performed blind to the condition of the experiments. Data distribution was assumed to be normal but this was not formally tested. No animals and data points were excluded from the analyses.

Data, reagent and code availability

The data that support the findings of this study are presented in the paper and the supplementary materials and all raw imaging data are available upon request. All routine analysis methods are included in the Methods section and MATLAB codes are deposited in github (https://github.com/gerardj-broussard/BroussardEtAl2018.git). Plasmids encoding axon-GCaMP and bicistronic variants (Accession numbers: MH282423, MH282424, MH282425, MH282426, MH282427, MH282429, MH282430, MH282432) have been made available in the Addgene plasmid repository (plasmid number 111261-112010).

Supplementary Material

Refer to Web version on PubMed Central for supplementary material.

Acknowledgments

This work was supported by funding to L. T. (DP2MH107056, U01NS090604, U01NS099714 from National Institute of Health and Rita Allen Foundation), to L.P. (Marie Curie PCIG12-GA-2012-334353, the European Union's Seventh Framework Program FP7/2007-2013 under grant agreement No. 600925, and the Champalimaud Foundation), to N. J. (Howard Hughes Medical Institute, and U01 NS103573, U01 NS103489 from National Institute of Health) and a Human Frontiers Research Grant to L.T. and L.P. (RGY0085/2013). We thank Dr. Huaiyang Chen at the vector core of vision center at UCD for virus production and Dr. Loren Looger and Dr. Brett Mensh for insightful comments on the manuscript.

References

1. Lin MZ & Schnitzer MJ Genetically encoded indicators of neuronal activity. Nat Neurosci 19, 1142–1153, doi:10.1038/nn.4359 (2016). [PubMed: 27571193]
2. Nakai J, Ohkura M & Imoto K A high signal-to-noise Ca2+ probe composed of a single green fluorescent protein. Nat Biotech 19, 137–141 (2001).
3. Tian L et al. Imaging neural activity in worms, flies and mice with improved GCaMP calcium indicators. Nature methods 6, 875–881, doi:10.1038/nmeth.1398 (2009). [PubMed: 19898485]
4. Akerboom J et al. Optimization of a GCaMP Calcium Indicator for Neural Activity Imaging. The Journal of Neuroscience 32, 13819–13840, doi:10.1523/jneurosci.2601-12.2012 (2012). [PubMed: 23035093]
5. Chen T-W et al. Ultrasensitive fluorescent proteins for imaging neuronal activity. Nature 499, 295–300, doi:10.1038/nature12354 (2013). [PubMed: 23868258]
6. Petreanu L et al. Activity in motor-sensory projections reveals distributed coding in somatosensation. Nature 489, 299–303, doi:10.1038/nature11321 (2012). [PubMed: 22922646]
7. Glickfeld LL, Andermann ML, Bonin V & Reid RC Cortico-cortical projections in mouse visual cortex are functionally target specific. Nat Neurosci 16, 219–226, doi:10.1038/nn.3300 (2013). [PubMed: 23292681]
8. Kaifosh P, Lovett-Barron M, Turi GF, Reardon TR & Losonczy A Septo-hippocampal GABAergic signaling across multiple modalities in awake mice. Nat Neurosci 16, 1182–1184, doi:10.1038/nn.3482 (2013). [PubMed: 23912949]
9. Gambino F et al. Sensory-evoked LTP driven by dendritic plateau potentials in vivo. Nature 515, 116–119, doi:10.1038/nature13664 (2014). [PubMed: 25174710]

10. Rothermel M & Wachowiak M Functional imaging of cortical feedback projections to the olfactory bulb. Frontiers in Neural Circuits 8, 73, doi:10.3389/fncir.2014.00073 (2014). [PubMed: 25071454]
11. Sun W, Tan Z, Mensh BD & Ji N Thalamus provides layer 4 of primary visual cortex with orientation- and direction-tuned inputs. Nat Neurosci 19, 308–315, doi:10.1038/nn.4196 (2016). [PubMed: 26691829]
12. Roth MM et al. Thalamic nuclei convey diverse contextual information to layer 1 of visual cortex. Nat Neurosci 19, 299–307, doi:10.1038/nn.4197 (2016). [PubMed: 26691828]
13. Kwon SE, Yang H, Minamisawa G & O'Connor DH Sensory and decision-related activity propagate in a cortical feedback loop during touch perception. Nat Neurosci 19, 1243–1249, doi:10.1038/nn.4356 (2016). [PubMed: 27437910]
14. Marques T, Nguyen J, Fioreze G & Petreanu L The functional organization of cortical feedback inputs to primary visual cortex. Nature Neuroscience 21, 757–764, doi:10.1038/s41593-018-0135-z (2018). [PubMed: 29662217]
15. Dreosti E, Odermatt B, Dorostkar MM & Lagnado L A genetically encoded reporter of synaptic activity in vivo. Nature methods 6, 883–889, doi:10.1038/nmeth.1399 (2009). [PubMed: 19898484]
16. Walker A, Burrone J & Meyer M Functional imaging in the zebrafish retinotectal system using RGECO. Frontiers in Neural Circuits 7, doi:10.3389/fncir.2013.00034 (2013).
17. El-Husseini Ael D, Craven SE, Brock SC & Bredt DS Polarized targeting of peripheral membrane proteins in neurons. The Journal of biological chemistry 276, 44984–44992, doi:10.1074/jbc.M103049200 (2001). [PubMed: 11546762]
18. Padmanabhan S, Kareva T, Kholodilov N & Burke RE Quantitative morphological comparison of axon-targeting strategies for gene therapies directed to the nigro-striatal projection. Gene therapy 21, 115–122, doi:10.1038/gt.2013.74 (2014). [PubMed: 24305419]
19. Kline CF, Scott J, Curran J, Hund TJ & Mohler PJ Ankyrin-B regulates Cav2.1 and Cav2.2 channel expression and targeting. The Journal of biological chemistry 289, 5285–5295, doi:10.1074/jbc.M113.523639 (2014). [PubMed: 24394417]
20. Aronov S, Aranda G, Behar L & Ginzburg I Axonal tau mRNA localization coincides with tau protein in living neuronal cells and depends on axonal targeting signal. The Journal of neuroscience : the official journal of the Society for Neuroscience 21, 6577–6587 (2001). [PubMed: 11517247]
21. Zlatkine P, Mehul B & Magee AI Retargeting of cytosolic proteins to the plasma membrane by the Lck protein tyrosine kinase dual acylation motif. Journal of cell science 110 (Pt 5), 673–679 (1997). [PubMed: 9092949]
22. Shigetomi E, Kracun S, Sofroniew MV & Khakh BS A genetically targeted optical sensor to monitor calcium signals in astrocyte processes. Nat Neurosci 13, 759–766, doi:10.1038/nn.2557 (2010). [PubMed: 20495558]
23. Lewis TL Jr., Mao T & Arnold DB A Role for Myosin VI in the Localization of Axonal Proteins. PLOS Biology 9, e1001021, doi:10.1371/journal.pbio.1001021 (2011). [PubMed: 21390300]
24. Kutzleb C et al. Paralemmin, a prenyl-palmitoyl-anchored phosphoprotein abundant in neurons and implicated in plasma membrane dynamics and cell process formation. The Journal of cell biology 143, 795–813 (1998). [PubMed: 9813098]
25. Lewis TL Jr., Mao T, Svoboda K & Arnold DB Myosin-dependent targeting of transmembrane proteins to neuronal dendrites. Nat Neurosci 12, 568–576, doi:10.1038/nn.2318 (2009). [PubMed: 19377470]
26. Bajar BT et al. Improving brightness and photostability of green and red fluorescent proteins for live cell imaging and FRET reporting. Scientific reports 6, 20889, doi:10.1038/srep20889 (2016). [PubMed: 26879144]
27. Hammond GRV, Sim Y, Lagnado L & Irvine RF Reversible binding and rapid diffusion of proteins in complex with inositol lipids serves to coordinate free movement with spatial information. The Journal of cell *biology* 184, 297–308, doi:10.1083/jcb.200809073 (2009).
28. de Chaumont F et al. Icy: an open bioimage informatics platform for extended reproducible research. Nat Meth 9, 690–696, doi:10.1038/nmeth.2075 (2012).

29. Koester HJ & Sakmann B Calcium dynamics associated with action potentials in single nerve terminals of pyramidal cells in layer 2/3 of the young rat neocortex. The Journal of Physiology 529, 625–646, doi:10.1111/j.1469-7793.2000.00625.x (2000). [PubMed: 11118494]
30. Hires SA, Tian L & Looger LL Reporting neural activity with genetically encoded calcium indicators. Brain cell biology 36, 69–86, doi:10.1007/s11068-008-9029-4 (2008). [PubMed: 18941901]
31. Guizar-Sicairos M, Thurman ST & Fienup JR Efficient subpixel image registration algorithms. Opt. Lett. 33, 156–158, doi:10.1364/OL.33.000156 (2008). [PubMed: 18197224]
32. Constantinople CM & Bruno RM Deep Cortical Layers are Activated Directly by Thalamus. Science (New York, N.Y.) 340, 1591–1594, doi:10.1126/science.1236425 (2013).
33. Petreanu L, Mao T, Sternson SM & Svoboda K The subcellular organization of neocortical excitatory connections. Nature 457, 1142, doi:10.1038/nature07709 (2009). [PubMed: 19151697]
34. Beierlein M & Connors BW Short-term dynamics of thalamocortical and intracortical synapses onto layer 6 neurons in neocortex. Journal of neurophysiology 88, 1924–1932 (2002). [PubMed: 12364518]
35. Zhao Y et al. An Expanded Palette of Genetically Encoded Ca(2+) Indicators. Science (New York, N.Y.) 333, 1888–1891, doi:10.1126/science.1208592 (2011).
36. Dana H et al. Sensitive red protein calcium indicators for imaging neural activity. eLife 5, e12727, doi:10.7554/eLife.12727 (2016). [PubMed: 27011354]
37. Nagai T, Yamada S, Tominaga T, Ichikawa M & Miyawaki A Expanded dynamic range of fluorescent indicators for Ca(2+) by circularly permuted yellow fluorescent proteins. Proc Natl Acad Sci U S A 101, 10554–10559, doi:10.1073/pnas.0400417101 (2004). [PubMed: 15247428]
38. Palmer AE et al. Ca2+ indicators based on computationally redesigned calmodulin-peptide pairs. Chemistry & biology 13, 521–530, doi:10.1016/j.chembiol.2006.03.007 (2006). [PubMed: 16720273]
39. Horikawa K et al. Spontaneous network activity visualized by ultrasensitive Ca(2+) indicators, yellow Cameleon-Nano. Nature methods 7, 729–732, doi:10.1038/nmeth.1488 (2010). [PubMed: 20693999]
40. Mank M et al. A genetically encoded calcium indicator for chronic in vivo two-photon imaging. Nature methods 5, 805–811, doi:10.1038/nmeth.1243 (2008). [PubMed: 19160515]
41. Thestrup T et al. Optimized ratiometric calcium sensors for functional in vivo imaging of neurons and T lymphocytes. Nature methods 11, 175, doi:10.1038/nmeth.2773 (2014). [PubMed: 24390440]
42. Marvin JS et al. An optimized fluorescent probe for visualizing glutamate neurotransmission. Nature methods 10, 162–170, doi:10.1038/nmeth.2333 (2013). [PubMed: 23314171]
43. Zhang F, Wang LP, Boyden ES & Deisseroth K Channelrhodopsin-2 and optical control of excitable cells. Nature methods 3, 785–792, doi:10.1038/nmeth936 (2006). [PubMed: 16990810]
44. Li H et al. Concurrent Imaging of Synaptic Vesicle Recycling and Calcium Dynamics. Frontiers in Molecular Neuroscience 4, 34, doi:10.3389/fnmol.2011.00034 (2011). [PubMed: 22065946]
45. Jackson RE & Burrone J Visualizing Presynaptic Calcium Dynamics and Vesicle Fusion with a Single Genetically Encoded Reporter at Individual Synapses. Frontiers in Synaptic Neuroscience 8, 21, doi:10.3389/fnsyn.2016.00021 (2016). [PubMed: 27507942]
46. Pech U, Revelo Natalia H., Seitz Katharina J., Rizzoli Silvio O. & Fiala A Optical Dissection of Experience-Dependent Pre- and Postsynaptic Plasticity in the Drosophila Brain. Cell reports 10, 2083–2095, doi:10.1016/j.celrep.2015.02.065.
47. Baden T et al. A Synaptic Mechanism for Temporal Filtering of Visual Signals. PLoS Biology 12, e1001972, doi:10.1371/journal.pbio.1001972 (2014). [PubMed: 25333637]
48. Dreosti E, Esposti F, Baden T & Lagnado L In vivo evidence that retinal bipolar cells generate spikes modulated by light. Nature neuroscience 14, 951–952, doi:10.1038/nn.2841 (2011). [PubMed: 21706020]
49. Johnston J, Ding H, Seibel SH, Esposti F & Lagnado L Rapid mapping of visual receptive fields by filtered back projection: application to multi-neuronal electrophysiology and imaging. The Journal of Physiology 592, 4839–4854, doi:10.1113/jphysiol.2014.276642 (2014). [PubMed: 25172952]

50. Cox CL, Denk W, Tank DW & Svoboda K Action potentials reliably invade axonal arbors of rat neocortical neurons. Proc Natl Acad Sci U S A 97, 9724–9728 (2000). [PubMed: 10931955]

Methods-only References

1. Kim JH et al. High Cleavage Efficiency of a 2A Peptide Derived from Porcine Teschovirus-1 in Human Cell Lines, Zebrafish and Mice. PLoS ONE 6, e18556, doi:10.1371/journal.pone.0018556 (2011). [PubMed: 21602908]
2. Tian L et al. Imaging neural activity in worms, flies and mice with improved GCaMP calcium indicators. Nature methods 6, 875–881, doi:10.1038/nmeth.1398 (2009). [PubMed: 19898485]
3. Lewis TL Jr., Mao T, Svoboda K & Arnold DB Myosin-dependent targeting of transmembrane proteins to neuronal dendrites. Nat Neurosci 12, 568–576, doi:10.1038/nn.2318 (2009). [PubMed: 19377470]
4. Kang M, Day CA, Kenworthy AK & DiBenedetto E Simplified equation to extract diffusion coefficients from confocal FRAP data. Traffic (Copenhagen, Denmark) 13, 1589–1600, doi: 10.1111/tra.12008 (2012).
5. Chen T-W et al. Ultrasensitive fluorescent proteins for imaging neuronal activity. Nature 499, 295–300, doi:10.1038/nature12354 (2013). [PubMed: 23868258]
6. de Chaumont F et al. Icy: an open bioimage informatics platform for extended reproducible research. Nat Meth 9, 690–696, doi:10.1038/nmeth.2075 (2012).
7. Pologruto TA, Sabatini BL & Svoboda K ScanImage: flexible software for operating laser scanning microscopes. Biomedical engineering online 2, 13, doi:10.1186/1475-925x-2-13 (2003). [PubMed: 12801419]
8. Sun W, Tan Z, Mensh BD & Ji N Thalamus provides layer 4 of primary visual cortex with orientation- and direction-tuned inputs. Nat Neurosci 19, 308–315, doi:10.1038/nn.4196 (2016). [PubMed: 26691829]
9. Petreanu L et al. Activity in motor-sensory projections reveals distributed coding in somatosensation. Nature 489, 299–303, doi:10.1038/nature11321 (2012). [PubMed: 22922646]
10. Kalatsky VA & Stryker MP New paradigm for optical imaging: temporally encoded maps of intrinsic signal. Neuron 38, 529–545 (2003). [PubMed: 12765606]
11. Marshel JH, Garrett ME, Nauhaus I & Callaway EM Functional Specialization of Seven Mouse Visual Cortical Areas. Neuron 72, 1040–1054, doi:10.1016/j.neuron.2011.12.004 (2011). [PubMed: 22196338]
12. Guizar-Sicairos M, Thurman ST & Fienup JR Efficient subpixel image registration algorithms. Opt. Lett. 33, 156–158, doi:10.1364/OL.33.000156 (2008). [PubMed: 18197224]
13. Koester HJ & Sakmann B Calcium dynamics associated with action potentials in single nerve terminals of pyramidal cells in layer 2/3 of the young rat neocortex. The Journal of Physiology 529, 625–646, doi:10.1111/j.1469-7793.2000.00625.x (2000). [PubMed: 11118494]
14. Anderson JS, Carandini M & Ferster D Orientation tuning of input conductance, excitation, and inhibition in cat primary visual cortex. Journal of neurophysiology 84, 909–926 (2000). [PubMed: 10938316]
15. Theer P & Denk W On the fundamental imaging-depth limit in two-photon microscopy. Journal of the Optical Society of America. A, Optics, image science, and vision 23, 3139–3149 (2006).

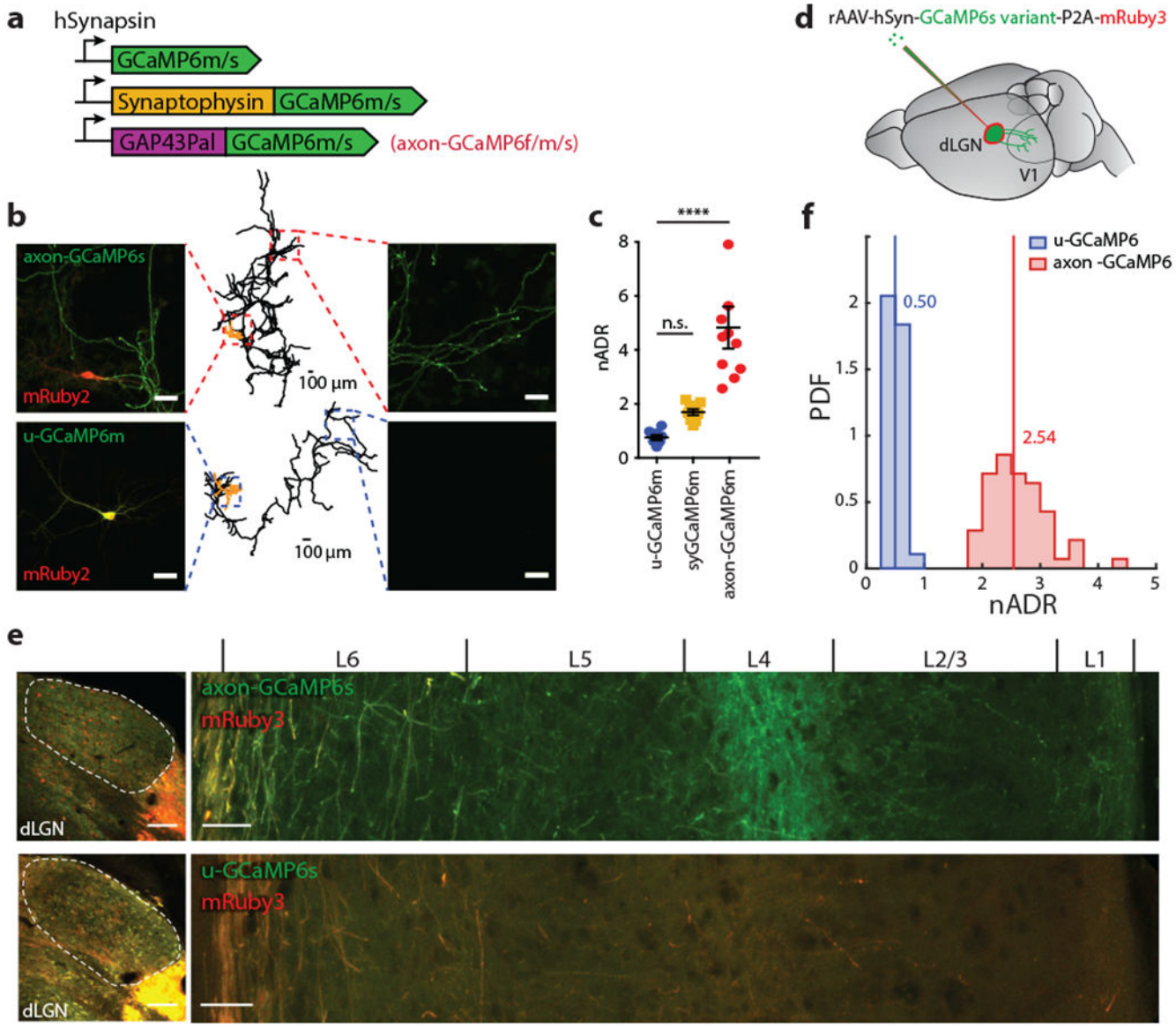

Figure 1: Axonal enrichement of GCaMP sensor driven by GAP43 targeting motif in dissociated cells and in vivo.

(**a**) Schematic representation of untargeted GCaMP6 (u-GCaMP6), vesicle protein synaptophysin-fused GCaMP6 (syGCaMP6) and GAP43-targeted GCaMP6 (axon-GCaMP6). (**b**) Representative images showing enhanced axon localization of axon-GCaMP6m compared to u-GCaMP6m in dissociated neuronal culture. Results were found to be consistent across 3 different cultures per construct. Scale bars: insets 20µm, cell traces 100µm. (**c**) Normalized Axon to Dendrite Ratio (nADR, see Methods for description). Average nADRs of axon-GCaMP6m (4.83±0.78) represent an approximate 5-fold increase compared to u-GCaMP6m (0.76±0.08) or syGCaMP6m (1.77±0.11). Data as mean ± s.e.m. F(2,27) = 26.52, P = 8.36E-7, n.s. = 0.23, ****P = 3.09E-5, One-way ANOVA with Tukey-Kramer multiple comparisons test; n = 8–10 cells from three cultures for each construct. (**d-f**) Characterization of ADR of thalamocortical axons in V1. (**d**) Schematic representation of

viral injection site of adeno associated virus encoding biscistronic constructs in mouse dLGN. (**e**) Representative images showing densely labeled L4 axons projected from dLGN labeled with axon-GCaMP6s, whereas cell somata were nearly devoid of labeling. Results were consistent across four animals per construct. Scale bars: 100μm (cortex), 500μm (thalamus). (**f**) Histogram of nADR values derived for both constructs with medians indicated by vertical line. Axon-GCaMP6s, 2.54±0.28; u-GCaMP6s, 0.50±0.06; data as median ± s.e.m.; P = 4.37E-16, Wilcoxon's rank-sum test; n = 56 slices analyzed for axon-GCaMP6s and n = 37 for u-GCaMP6s from 3 animals per construct.

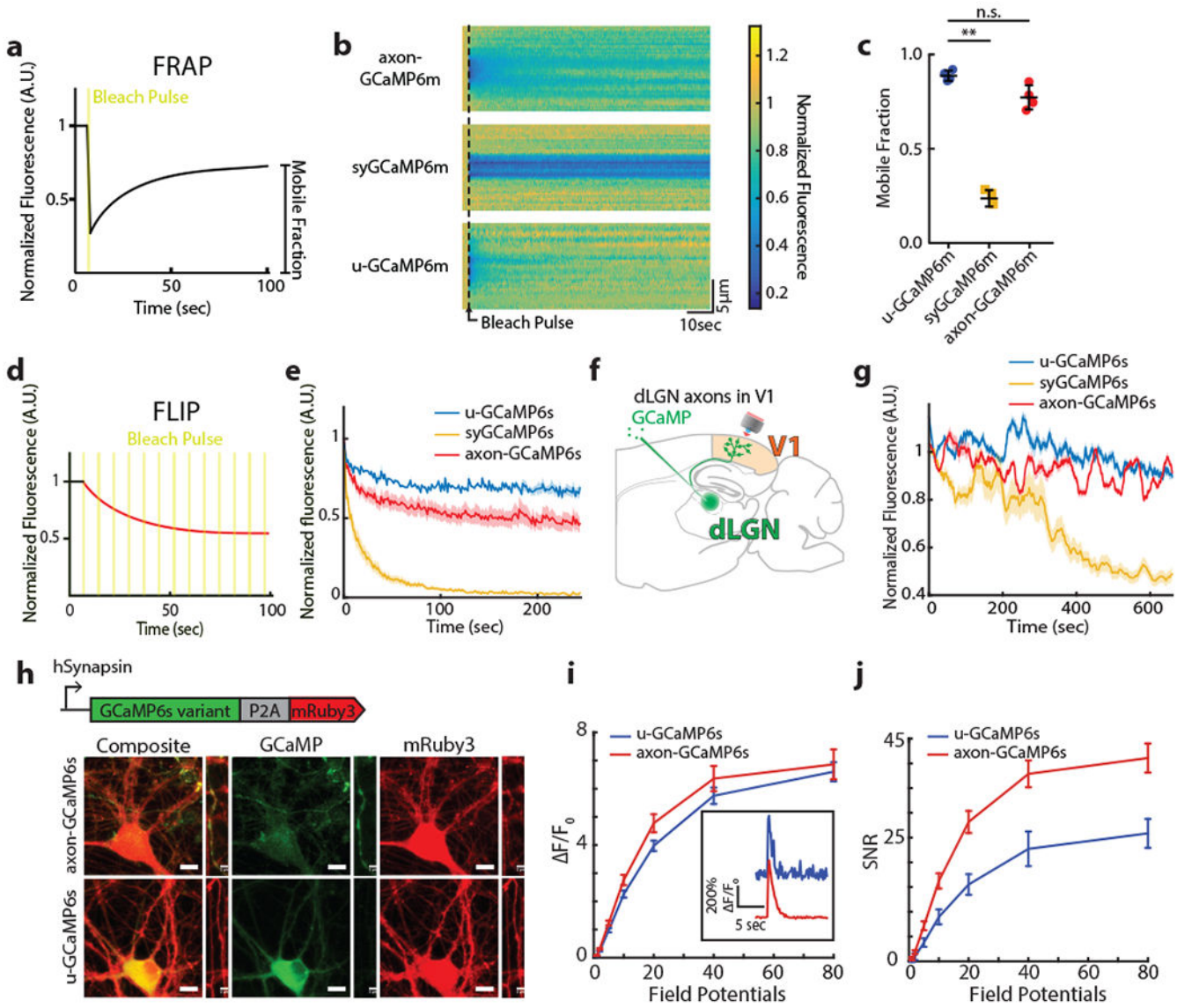

Figure 2: Axon-GCaMP maintains photostability and displays enhanced SNR.

(**a-e**) Characterization of photostability and diffusibility. Schematic representation of the FRAP (**a**) and FLIP (**d**) experiments. (**b**) Representative pseudo-linescans from u-GCaMP6m, axon-GCaMP6m, and syGCaMP6m FRAP demonstrated rapid recovery of fluorescence for uGCaMP6m and axon-GCaMP6m, but not in the case of the syGCaMP6m. Experiment was repeated on two independent cultures per construct with similar results. (**c**) Mobile fraction of uGCaMP6m, syGCaMP6m, and axon-GCaMP6m as assessed by FRAP. Data plotted as mean ± s.e.m. $X^2(2,11) = 9.85$, P = 0.0073; *n.s. = 0.26, ***P = 0.0048, Kruskal-Wallis test with Dunn's test for multiple comparisons; n = 4 cells from 2 plates per construct. (**e**) Time course of normalized fluorescence intensity changes during FLIP experiments. Data plotted as mean (solid line) ± s.e.m. (shaded regions); n = 3 cells per construct. (**f-g**) Characterization of photostability in vivo. (**f**) Schematic representation of viral injection in dLGN followed by *in vivo* imaging axons projecting to V1. (**g**) Time

course of fluorescence intensity normalized to the first 50 seconds of acquisition during imaging of dLGN projection. Data plotted as mean (solid line) ± s.e.m. (shaded regions); n = 377, 70, and 236 for u-GCaMP6s, syGCaMP6s, and axon-GCaMP6s, respectively. Individual traces were smoothed by a 100 time-point boxcar filter to emphasize low frequency components of data. (**h**) (top) Schematic representation of bicistronic constructs expressed in dissociated neuronal culture. (bottom) Representative images showing increased green fluorescence in axons when labeled with axon-GCaMP6m, whereas u-GCaMP6m primarily labels somato-dedritic compartments of neurons. Experimental data was derived from 3 independent cultures per construct with similar results. Scale bar: somatic image 10μm, axonal image 3μm. (**i-j**) Average ΔF/F (**i**) and SNR (**j**) in response to indicated number of field potential stimuli. Inset shows reduced baseline noise in single-trial time-lapse traces of axon-GCaMP6s in response to 20FP stimuli. Data plotted as mean peak values ± s.d.; n = 9 imaging sessions from 3 transductions per construct.

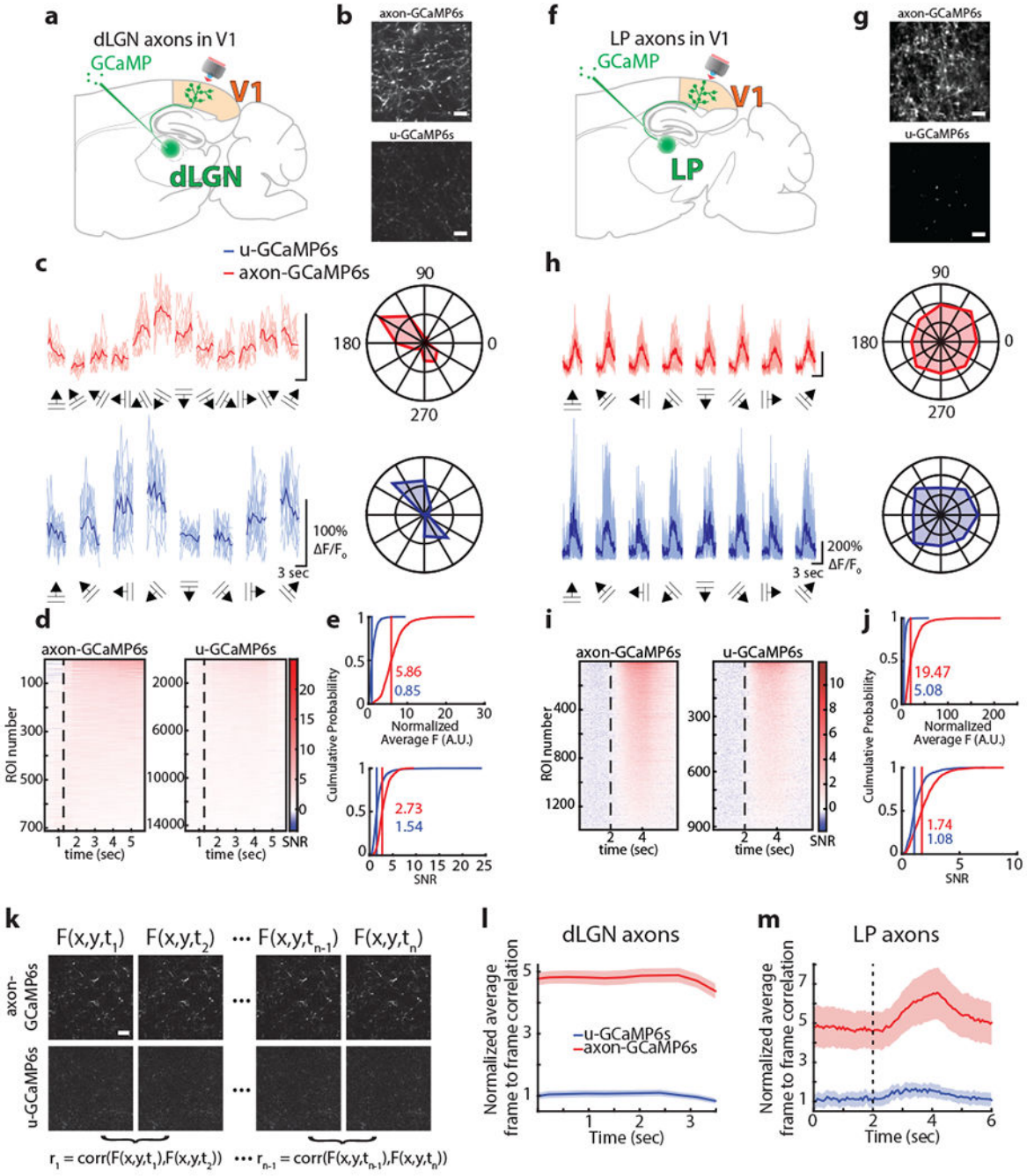

Figure 3: Axon-GCaMP6s improves SNR and image-wise correlations in long-distance axons.

(**a, f**) Schematic representation of viral injection in dLGN (**a**) and LP (**f**), followed by *in vivo* imaging in V1 of projected axons. (**b, g**) Representative images of L1 axons projected from dLGN (**b**) and LP (**g**) demonstrating enhanced brightness of axon-GCaMP6s expressing axons. Experiments were performed in at least 3 animals per construct injection site pair with similar results. Scale bars:10 μm. (**c,h**) (left) Fluorescence of a representative ROI in response to the indicated grating directions (10 trials per direction) of axon-GCaMP6s and u-GCaMP6s in dLGN (**c**) and LP (**h**). Data presented with averages in dark colors and

individual trials in light colors. Scale bars 3 seconds, 100% ΔF/F. (right) Polar plots of tuning properties of the selected ROIs. (**d, i**) Trial-averaged traces of SNR time course from all responsive ROIs to preferred stimulus direction. Point at which moving stimulus presented indicated by vertical dotted black line. (**e, j**) (top) Cumulative distribution of normalized fluorescence intensity of axon-GCaMP6s and u-GCaMP6s in dLGN (**e**) and LP (**j**) axons projecting to V1. (dLGN: axon-GCaMP6s, 5.85; u-GCaMP6s, 0.85; LP: axon-GCaMP6s, 19.47; u-GCaMP6s, 5.08; P = 2.15E-259 and 1.24e-319, respectively by the Kolmogorov-Smirnov test). (bottom) Cumulative distribution of SNR of individual ROIs with median values indicated by vertical lines as well as color-coded numeric values (dLGN: axon-GCaMP6s, 2.73; u-GCaMP6s, 1.54; LP: axon-GCaMP6s, 1.07; u-GCaMP6s, 0.64; P = 9.56E-130 and 1.13E-95, respectively by the Kolmogorov-Smirnov test). For (**e**) n=712 ROIs from 4 animals for axon-GCaMP6s and n=14478 ROIs for u-GCaMP6s from 19 animals. For (**j**) n=1393 ROIs from 3 animals for axon-GCaMP6s and n=917 ROIs from 4 animals for u-GCaMP6s. (**k-m**) axon-GCaMP6s improves frame to frame correlations. (**k**) Representative frames from one imaging session per construct in L1 dLGN experiments showing enhancements to image structure for axon-GCaMP6s. The text above and below the images demonstrates the procedure for calculating the frame-to-frame correlations. Scale bar: 10μm. (**l, m**) Axon-GCaMP6s permits significantly improved frame-to-frame correlations for image registration. Time course of image-wise correlation values for dLGN (**l**) and LP (**m**) boutons. Data plotted as mean (solid line) ± s.e.m. (shaded regions); n = 6 imaging sessions from two animals for each construct.

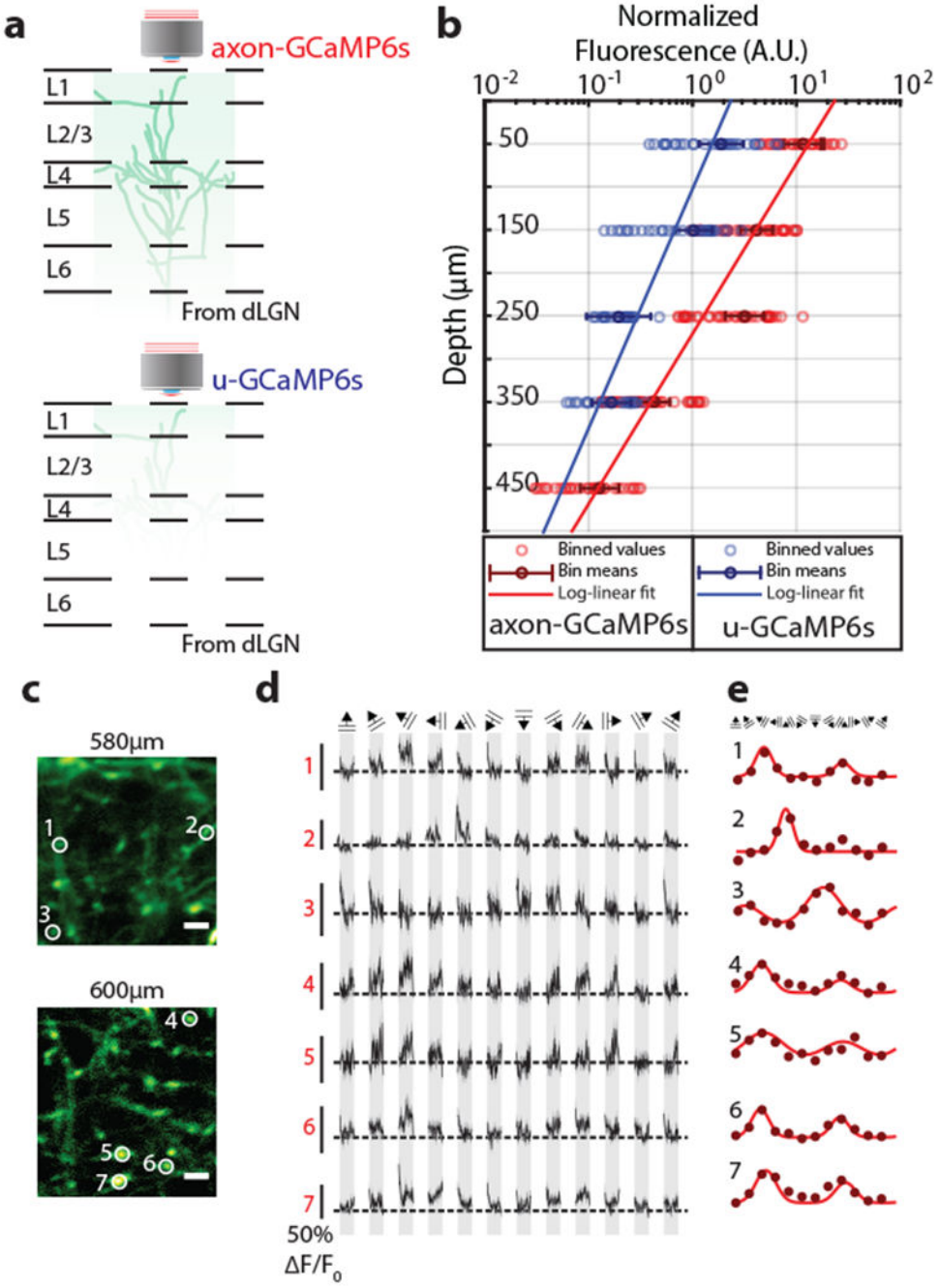

Figure 4: Imaging thalamocortical afferents deep in cortical tissue with axon-GCaMP6s

(**a**) Experimental schematic demonstrating that brighter axon-GCaMP6s axons can be imaged at deeper layers within tissue than u-GCaMP6s axons. (**b**) Comparison of axon-GCaMP6s and u-GCaMP6s fluorescence normalized to the square of the excitation laser power as a function of imaging depth (Data plotted as individual ROIs with binned values (light color) and binned means ± s.e.m (dark colors), and log-linear fit across the depth). $F(1,1396) = 1242.35$, $P < 4.94E\text{-}324$, ANCOVA. For u-GCaMP6s we analyzed 500 ROIs from 2 imaging sessions per depth from each of 4 animals, for axon-GCaMP6s 900 ROIs

from 2 imaging sessions per depth from 3 animals. (**c**) Representative images of dLGN axons projecting to V1 with overlays indicating analyzed ROI location at 580μm (top) and 600μm (bottom) below pia. Results were similar across three tested animals. Scale bars 3 μm. (**d-e**) Response properties of individual ROIs deep in tissue. (**d**) Average ΔF/F traces aligned to stimulus direction of ROIs indicated in (**c**) with baseline indicated by dotted black line. Data plotted as mean (black line) ± s.e.m. (gray shading). n = 10 trials per direction. (**e**) Tuning curves for individual ROIs.

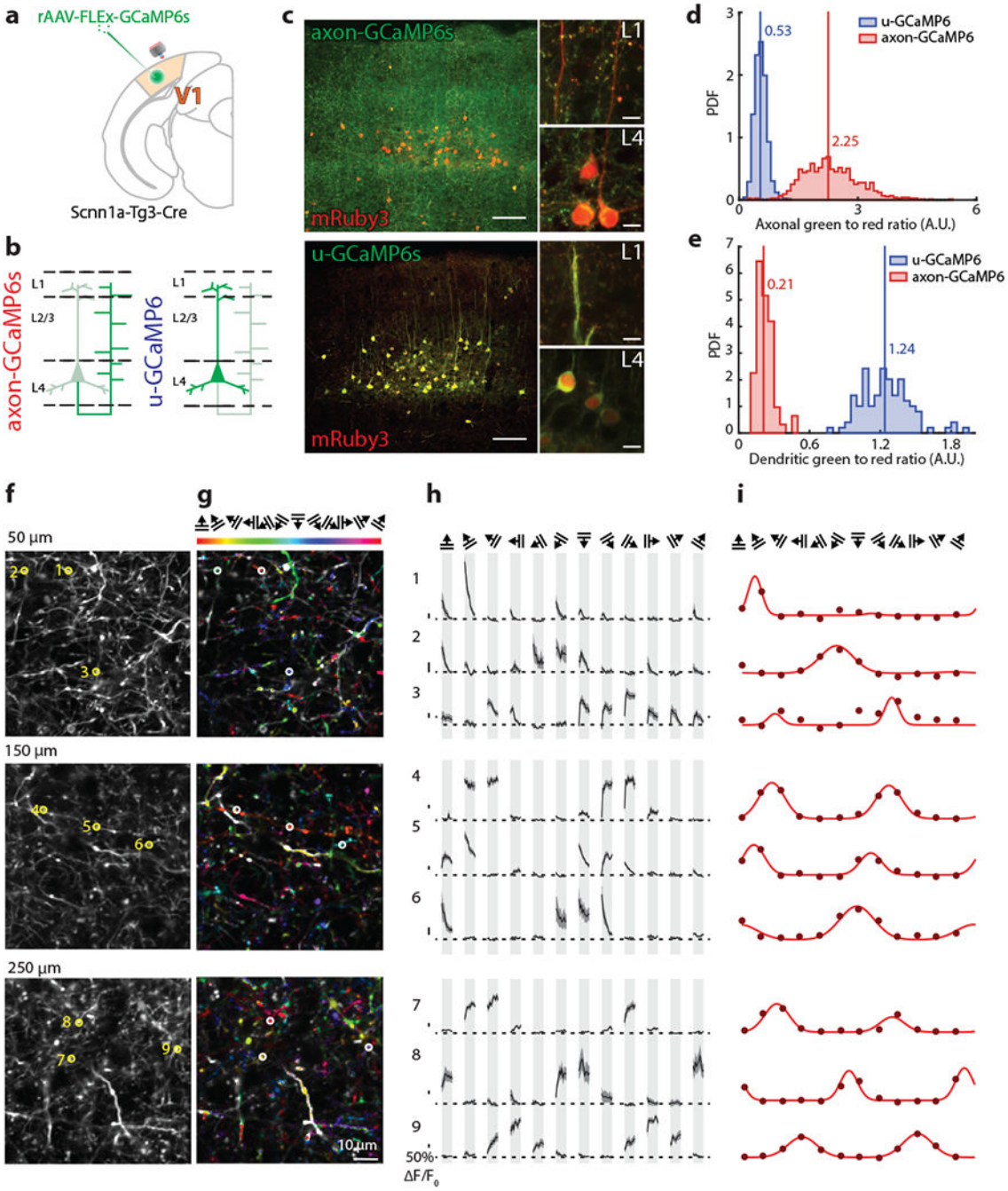

Figure 5: Axon-GCaMP6s permits layer specific recording of axons projected from local neurons without contamination from somatodendritic signals.

(**a**) Schematic representation of labeling L4 neurons with Cre-dependent adeno associated virus encoding axon-GCaMP6s or u-GCaMP6s in *Scnn1a-Cre*-Tg3 mice. (**b**) Expected pattern of transduction: axon-GCaMP6s strongly labeling axons with weak labeling in the somatodendritic compartment and the reverse pattern for u-GCaMP6s. (**c**) Representative images showing expression patterns of axon-GCaMP6s (top) or u-GCaMP6s (bottom) fused to P2A-mRuby3. Axon-GCaMP6s is enriched in axons, whereas u-GCaMP6s more strongly

labels somatodendritic compartments. Inset shows representative zoomed-in images in L1 and L4. This result was consistently found in two animals per construct. Scale bar: somatic image 100μm, inset images 10μm. (**d-e**) Distributions of green-to-red ratio at axons (**d**) or dendrites (**e**). Distribution medians indicated by vertical lines. Axon-GCaMP6s displayed significantly enhanced green-to-red ratio in axons, but dramatically decreased green-to-red ratio in dendrites, compared to u-GCaMP6s. $P < 4.94E-324$ and $P = 1.57E-26$, Wilcoxon's rank sum test; data from n = 1200 ROIs from 2 animals for both constructs. (**f-i**) Axon-GCaMP6s enabled layer-specific tuning properties of axons across cortical layers in V1. Data were derived from 2 imaging sessions per depth in 2 animals. (**f**) Representative images of axons at indicated depth with overlays indicating analyzed ROIs. (**g**) Color-coded tuning map demonstrating pixel-wise tuning across analyzed images. (**h**) Average ΔF/F traces aligned to stimulus direction of individual ROIs with baseline indicated by dotted black line. Data plotted as mean (black line) ± s.e.m. (gray shading). n = 10 trials per direction. (**i**) Tuning curves for individual ROIs.